RSC Advances

PAPER

View Article Online
View Journal | View Issue

Cite this: *RSC Adv.*, 2016, **6**, 57727

Tailoring the multiferroic behavior in $BiFeO_3$ nanostructures by Pb doping

Kuldeep Chand Verma*[a] and R. K. Kotnala[b]

Received 18th May 2016
Accepted 24th May 2016

DOI: 10.1039/c6ra12949h

www.rsc.org/advances

The weak and deficient manipulation of charge–spin coupling in multiferroic $BiFeO_3$ (BFO) notoriously limits device applications. To mould the spontaneous charge and the spin orientation synergistically in BFO, in this paper Pb^{2+} substitution for Bi^{3+} could induce lattice distortions and structural phase transitions to tune the lone-pair activity ($6s^2$) for ferroelectricity and neutralized oxygen vacancies to valence Fe^{2+}/Fe^{3+} superexchange for ferromagnetism. Multiferroic $Bi_{1-x}Pb_xFeO_3$ [$x = 0$, 0.05, 0.075 and 0.1] nanostructures were synthesized by a chemical combustion process. X-Ray diffraction confirms the distorted rhombohedral BFO structure and the lattice expansion with Pb doping. The Pb ions also modified the shape of the BFO nanostructures. The observed ferroelectric behavior depends upon lattice distortion, reduction in oxygen vacancies to induce low leakage current and the shape/size effect in BFO nanostructures. The zero field (ZFC) and field cooling (FC) SQUID measurement confirm the strength of antiferromagnetism in BFO with Pb^{2+} ions. The cusp in ZFC magnetization is studied by ac magnetic susceptibility measurements that include spin-glass and superparamagnetic interactions in antiferromagnetism at low temperature. The oxidation states in BFO suggest oxygen vacancies that are reduced with Pb doping and maintain Fe^{2+}/Fe^{3+} valences. The dielectric permittivity changes with applied dc magnetic field, which could induce a magnetodielectric effect due to spin pair correlation of neighboring spins and the coupling constant. Furthermore, significant dielectric anomalies appear near both the ferroelectric phase transition, and the Neel temperature of BFO implies the magnetoelectric coupling.

1. Introduction

Multiferroics have recently motivated researchers to understand the potential applications and driving mechanisms that are responsible for magnetoelectric coupling (ME), including:[1–4] (i) the electrostriction-induced strain variation in ferromagnetic ions, changing its lattice and associated magnetic properties; (ii) the delicate modulation of carrier density by polarization reversal in ferroelectric field-effect transistor that motivates the ferromagnetic/antiferromagnetic phase transition; (iii) the use of multiferroic materials which provides a route to electrical control of spin arrangement by ferromagnetic/antiferromagnetic exchange coupling. The electrostriction and exchange coupling need higher ferroelectric polarization and multiferroicity, respectively, while the carrier modulation only has significance in ferromagnetic/antiferromagnetic phase transitions. Over the past decade, various multiferroic systems such as $BaTi_2O_4$, $YMnO_3$, $BiMnO_3$, $LuFe_2O_4$, and $BiFeO_3$ have been widely studied.[5] Among them, $BiFeO_3$ (BFO) with high $T_c \sim$ 1103 K and $T_N \sim$ 643 K attracts much attention because it has simultaneously ferroelectric and antiferromagnetic properties even at room temperature. This is since the ferroelectricity in BFO originates from the $6s^2$ lone pair electrons of Bi^{3+} ions due to structural distortion, while the magnetism occurs by Fe–O–Fe superexchange interactions.[6]

As an overview, BFO has a disappointingly low spontaneous polarization and saturation magnetization due to the superimposition of a spiral spin structure on BFO that could be attributed to the antiferromagnetic order.[7] In this spiral spin structure, the antiferromagnetic axis rotates through the crystal with an incommensurate long-wavelength period of 62 nm, which cancels the macroscopic magnetization and also inhibits ME coupling. Hence, for novel electronics of BFO, its magnetic and electric properties must be enhanced. The superexchange between the octahedrally coordinated Fe^{3+} through the O ligand is responsible for the antiferromagnetism, but $BiFeO_3$ has been reported to have a weak ferromagnetic component at room temperature and is thus canted, with a helical repeat of ~620 Å.[8] The presence of oxygen vacancies and the valence fluctuation (Fe^{2+}/Fe^{3+}) are believed to be the main disadvantages causing large electrical leakage in BFO.[9] The substitution of Pb ions at the Bi-site would induce more buckling in the Fe–O–Fe bond angle accompanying a smaller tolerance factor that would lead

[a]*Centre of Advanced Study in Physics, Department of Physics, Panjab University, Chandigarh 160 014, India. E-mail: kuldeep0309@yahoo.co.in; dkuldeep.physics@gmail.com; Tel: +91-9418941286*

[b]*CSIR-National Physical Laboratory, New Delhi 110012, India*

to a more insulating character. Also, doping with the higher valence Ti ion in BFO is an effective way to obtain a stable perovskite phase with neutralized defect carriers. Qi *et al.*[10] suggested that a donor dopant such as Pb^{2+} ions for the A-site Bi^{3+} of BFO could reduce Fe^{3+} to Fe^{2+} ions, which are presumably compensated by oxygen vacancies.

Recently, there have been various multiferroic BFO systems that are responsible for the enhancement of ferroelectricity and ferromagnetism.[11–15] Rout *et al.*[13] substitutes Ba^{2+} for Bi^{3+} due to oxygen vacancies which affect the centro-symmetry of FeO_6 octahedra that would lead to a change in magnetic behavior. Chang *et al.*[2] suggested that the substitution of Ba^{2+} for Bi^{3+} could suppress the spiral spin configuration of antiferromagnetic BFO due to larger ionic size of Ba ions. However, Wei *et al.*[14] suggested that the Bi^{3+} ions drive structural distortion and thus the ferroelectricity through its $6s^2$ lone pair in BFO. Moreover, the substitution for Bi^{3+} in BFO can increase distortions in the FeO_6 octahedra and Fe–O–Fe bond angles and, thus, the tetragonality in the crystal structure.[6] The resultant chemical strain from these structural variations can augment the polar displacement of Bi^{3+} ions and the $6s^2$ lone pair electrons of Bi^{3+} ions; as a result increased polarization is expected.[15]

In the present paper, we have reported the structural, nanostructural, ferroelectric, magnetic, oxidation state, dielectric and ME properties of multiferroic $Bi_{1-x}Pb_xFeO_3$ [x = 0 (BFO), 0.05 (BPFO5), 0.075 (BPFO75) and 0.1 (BPFO10)] nanostructures.

2. Experimental details

The $Bi_{1-x}Pb_xFeO_3$ (Pb:BFO) nanostructures were prepared by chemical combustion using bismuth nitrate, lead nitrate, ferric nitrate, polyethylene glycol (PEG) and urea taken in a desired stoichiometric ratio of BFO, BPFO5, BPFO75 and BPFO10. To prepare a precursor solution, bismuth nitrate, lead nitrate and ferric nitrate were added in PEG and kept stirring while raising the room temperature to 50 °C. An additional 20 mol% excess of Pb was also added to compensate for the Pb loss during processing and to assist crystallization. Urea was added and the temperature was then raised to 70 °C till combustion took place. The nitrates acted as oxidising agents, and PEG and urea were reducing agents. The brown powder so-obtained was purified by washing with a mixture of ethanol and water (double distilled) and finally subjected to annealing at 500 °C for 5 h.

The crystalline structure was analyzed by X-ray diffraction (XRD) with a step size of 0.02° and Cu Kα (1.5418 Å) radiation on an X'Pert PRO system. The microstructure was confirmed by field-emission scanning electron microscopy (FESEM) on an SU8010 system. Magnetization measurements were performed on a Quantum Design SQUID VSM for the temperature, T = 5–300 K and magnetic field, H = −5 to +5 kOe. For electrical measurements, the Pb doped BFO crystalline powder was pressed into pellets (thickness ∼ 0.5 mm and radius ∼ 5 mm) with a pressure of 5 bar/10 min and then sintered at 1000 °C/5 h. Polarization under the influence of electric field was measured using a Radiant Technologies ferroelectric test system. The current–voltage measurements were carried out using a source meter (Keithley 2611 system). The real, $\chi'_{ac}(T)$, component of the complex ac magnetic susceptibility, $\chi_{ac}(T)$, measurement was done with a Quantum Design magnetometer using an oscillating field, H_{ac} = 2.5 Oe for frequencies 1 Hz, 100 Hz, 1 kHz and 10 kHz at T = 5–200 K, without any dc field bias. Samples were measured from a demagnetized state, cooling in zero field with no dc field applied to maximize the ac signals. It is to be noted that a small enough ac magnetic field, H_{ac}, enables us to measure the true spin susceptibility of a magnetic system. The limit of this field is again determined by the sensitivity of the setup itself. X-Ray photoelectron spectroscopy (XPS) was performed using a Perkin-Elmer model 1257.

The change in relative dielectric permittivity as a function of an applied frequency under the influence of magnetic field strength (H = 0, 1 kOe) was measured. For this, a sample pellet with electrodes was put onto the holder of a VSM (7304 Lakeshore) system. A magnetic field was applied through the VSM system and the corresponding capacitance was measured by a Wayne Kerr 6500B Precision Impedance analyzer. The magnetic field was applied along the pellet thickness and the dielectric constant was also measured along the thickness direction (longitudinal mode). Details are given elsewhere.[16]

3. Result and discussion

Fig. 1 shows the XRD patterns of the Pb:BFO nanostructures measured at room temperature. The reflection peaks of the pure BFO sample can be indexed to a rhombohedral structure with space group *R3c* (JCPDS card: 71-2494). This is based on the character of the single (012) peak at around 22° and the splitting of the (104) and (110) peaks around 32°. The splitting of XRD peaks indicate the structural distortion due to the tilting of FeO_6 octahedrons.[17] The Pb doped BFO samples also maintains a rhombohedral structure, which is manifested by the splitting of the (006) and (202) peaks around 40°. No additional peaks were observed in the XRD patterns, confirming the crystalline

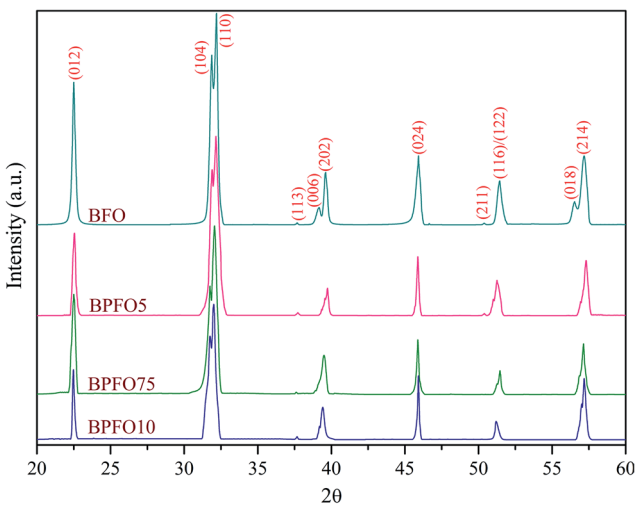

Fig. 1 XRD pattern of $Bi_{1-x}Pb_xFeO_3$ [x = 0 (BFO), 0.05 (BPFO5), 0.075 (BPFO75) and 0.1 (BPFO10)] multiferroic systems.

Table 1 Values of lattice constants and nanostructural dimensions [diameter (D) and length (L)] for $Bi_{1-x}Pb_xFeO_3$ multiferroic systems

Sample	a/Å	c/Å	c/a	V/Å^3	D/nm	L/nm
BFO	5.578	13.862	2.4851	373.5088	75 ± 2	—
BPFO5	5.577	13.893	2.4911	374.2098	400 ± 15	—
BPFO75	5.573	13.905	2.4951	373.996	102 ± 5	510 ± 15
BPFO10	5.574	13.915	2.4964	374.3993	125 ± 4	900 ± 20

phase of the pure BFO. The calculated lattice constants (given in Table 1) are in agreement with rhombohedral BFO nanoparticles.[18] The increase in lattice constant, c and decrease a may change in those Fe–O bond lengths and Fe–O–Fe bond angles which have a significant effect on the multiferroic properties.[19] The values of the distortion ratio, c/a = 2.4851, 2.4911, 2.4951 and 2.4964, and unit cell volume, V (Å^3) = 373.5088, 374.2098, 373.996 and 374.3993, respectively, for BFO, BPFO5, BPFO75 and BPFO10. The enhancement in the value of V supports the idea that Pb doping induces strain in the BFO and expands the unit cell.[20] The variation in the a and c lattice constant values with Pb doping indicate a distortion/strain in the BFO structure.

Moreover, with the doping of Pb^{2+} ions in BFO, the intensity of the XRD peaks is reduced which indicates the incorporation of a dopant into the host lattice. The Pb^{2+} substitution in BFO is also confirmed by peak shifting to a lower diffraction angle, indicating an expansion of the lattice, because the dopant Pb^{2+} (1.29 Å) has a larger ionic size than Bi^{3+} (1.17 Å). The structural transformations are seen due to peaks (104/110), (006/202) and (018/214) merging together with increasing Pb^{2+} ions concentration which indicates coalescence behavior. The reduction in peak splitting indicates a structural transition of tetragonal BFO.[21] This implies the existence of huge internal strain developed inside the multiferroic samples when undergoing the structural phase transition from the rhombohedral to tetragonal phase upon doping, with lattice distortion to induce ferroelectricity.[22] Thus, the lattice strain is represented in terms of rhombohedral to tetragonal splitting, lattice distortion and unit cell expansion which might influence the resulting multiferroic behaviors. Recently, it has been reported that the lattice strain could increase the transition temperatures to induce phase changes, and modify the anisotropic symmetry to influence polarization, dielectric permittivity and piezoelectric responses.[23] The lattice strains are attributed to a transition between cycloidal and homogeneous antiferromagnetic spin states, releasing a latent antiferromagnetic component locked within the cycloid.

Fig. 2(a–d) shows the FESEM images of Pb:BFO nanostructures. It is shown that the dopant Pb ions are highly influenced by the morphology of pure BFO. Nanoparticles of average diameter, D = 75 ± 2 nm are calculated for pure BFO. However, the 5% Pb dopant ions in Bi^{3+} (BPFO5) have a cubic-shaped nanoparticle morphology (D = 400 ± 15 nm); the higher dopant level of 7.5 and 10% Pb in Bi^{3+} shows an anisotropic morphology, such as nanorod-like formations. The diameters of the nanorods, D = 102 ± 5 nm and 125 ± 4 nm,

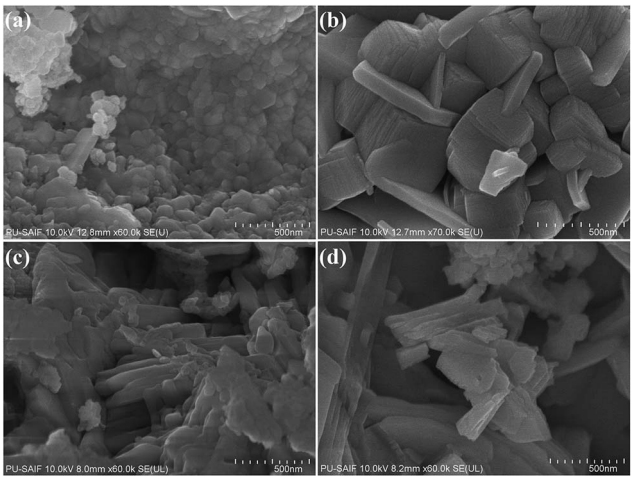

Fig. 2 FESEM images (a) BFO (b) BPFO5 (c) BPFO75, (d) BPFO10.

and lengths, L = 510 ± 15 nm and 900 ± 20 nm, respectively, for BPFO75 and BPFO10. In all the BFO nanostructures, we have observed that the average grain size (D & L values) increases with increased Pb doping. This is explained due to larger ionic size of Pb^{2+} ions than Bi^{3+}. The mechanism of morphological variation with Pb doping in BFO is explained due to variation in the valence states of Fe ions due to oxygen vacancies. The substitution of Pb^{2+} into Bi^{3+} ions induces Fe^{2+}/Fe^{3+} ions in the BFO matrix that can influence lattice defects (oxygen vacancies) to enhance the surface energy of the rhombohedral BFO. This results in quick anisotropic growth along the c-axis. This type of behavior is described by Iqbal *et al.*[24] The dopant effect on valence states due to vacancy formation is also expected to affect the morphology (shape/size) of the particle.[25]

The oxide perovskites do not all have the same mechanism of ferroelectricity: the center Ti ion plays a key role in $BaTiO_3$ but the lone-pair Pb ion is dominant in $PbTiO_3$.[26] Indeed, this seems to be the case in BFO, where the polarization is mostly caused by the lone pair of Bi^{3+}, so that the polarization comes mostly from the A-site while the magnetization comes from the B site (Fe^{3+}).[27] The lone-pair orbital of Bi^{3+} ($6s^2$) is stereochemically active and responsible for ferroelectric distortion. Here, the distortion is induced by Pb doping and therefore, by tuning the lone-pair activity. Fig. 3(a′–d′) shows a room temperature polarization–applied electric field (P–E) hysteresis for BFO samples measured at 50 Hz. All samples exhibit well-saturated ferroelectric hysteresis with the value of spontaneous polarization, P_s is 0.75, 1.76, 3.55 and 6.73 μC cm^{-2}, respectively, for BFO, BPFO5, BPFO75 and BPFO10 nanostructures. The values of remanent polarization (P_r) with coercivity (E_c) are also given in Table 2. It has also observed that the value of P_r is enhanced because the doping of Pb^{2+} for Bi^{3+} requires charge compensation, which usually neutralized the oxygen vacancies [Fig. 6] and it results in a split of Fe^{3+} to Fe^{2+}. In pure BFO, the nanoparticles have smaller size as compared to the bulk sample, the grain boundary is larger, the leakage current is increased, and the polarization behavior is degraded. Generally, the ferroelectric behavior is weakened due to the increase in oxygen

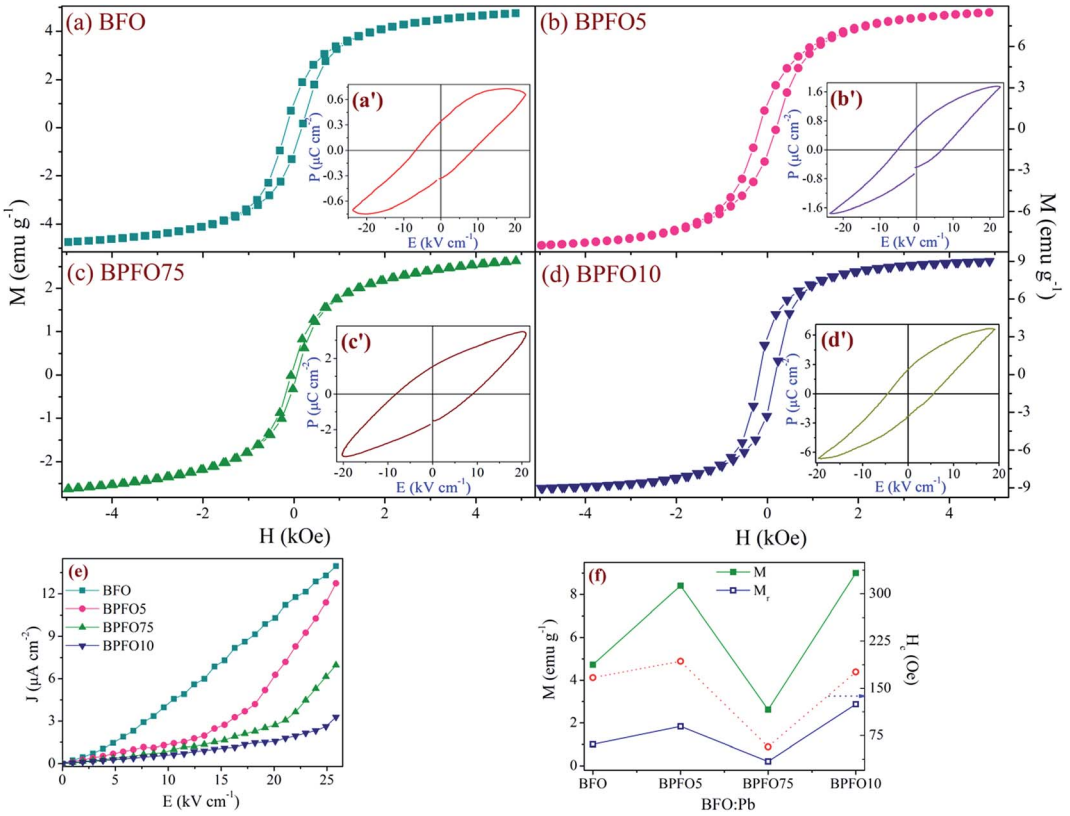

Fig. 3 (a–d) Magnetization–applied field (M–H) measurement at room temperature for Pb:BFO multiferroic systems. Insets (a′–d′) shown polarization–electric field (P–E) hysteresis, respectively, measured at room temperature. (e) Leakage current as the function of applied electric field. (f) Plot of M, M_r and H_c with varying the concentration of Pb in BFO multiferroic systems.

vacancies that form more free electrons resulting in a higher conductivity and hence have a harmful influence on the ferroelectricity.[28] In ferroelectric materials, domain-wall mobility is one of the contributing factors to the polarizability. The domain-wall interacts with the defects, such as oxygen vacancies, generating domain-wall pinning. The pinning of the domain walls restricts the polarization switching, giving rise to lower remanent polarization. In the present samples [Fig. 3(a′–d′)], the ferroelectricity is enhanced with Pb doping due to a reduction in the oxygen vacancies of BFO and these vacancies are not only influenced by Pb^{2+} ions but the shape/size effect also. The Pb doping into BFO could increase the grain size as well the oriented growth (nanorod-type) in the samples. A small grain size means a large number of grain boundaries, which led to a polarization discontinuity between grains and hence decreased polarization.[29] For oriented growth (nanorods), the surface-to-volume ratio becomes higher. The surface compressive stress caused by nanorods (1 dimensional nanostructure) produces an effective tensile in the length direction.[30] This leads to a big off-center atomic displacement. The 1D nanostructure has a uniaxial tensile stress, and if it is applied along the c-axis an enhancement in ferroelectricity as well piezoelectric strain is possible.[31] Moreover, the Pb substitutions increase the distortions in the FeO_6 octahedral and Fe–O–Fe bond angles, and thus, the distortion in the crystal structure. The observed ferroelectric polarization is not much enhanced with Pb doping when compared with BFO multiferroic systems that have been recently reported.[29,32,33] The small polarization here relates to

Table 2 Values of spontaneous polarization (P_s), remanent polarization (P_r), electric coercivity (E_c), current density (J) at 20 kV cm^{-1}, dielectric constant (ε) and MC at 1 kHz and 1 MHz, and ferroelectric phase transition (T_{FE}) at 1 MHz for $Bi_{1-x}Pb_xFeO_3$ nanostructures

Sample	P_s/μC cm^{-2}	P_r/μC cm^{-2}	E_c/kV cm^{-2}	J/μA cm^{-2}	ε		MC (%)		T_{FE}/K
					1 kHz	1 MHz	1 kHz	1 MHz	
BFO	0.75	0.35	7.66	10.31	6.2	5.1	0.68	0.61	644
BPFO5	1.76	0.63	6.03	6.27	1.9	1.8	2.56	1.59	631
BPFO75	3.55	1.57	8.55	2.72	13	10.6	3.61	0.36	649
BPFO10	6.73	2.63	5.06	1.57	34	12	0.86	0.11	629

the residual oxygen vacancies that may not neutralized by dopant ions. Another dopant, such as higher valence Ti ions (along B-site) for Fe^{3+}, may stabilize the BFO structure with a low leakage of current.[9] However. the oxygen vacancies play an important role in ferromagnetism enhancement that will be discussed in the following paragraphs.

In order to understand the mechanism of the observed ferroelectric behavior [Fig. 3(a′–d′)], the leakage currents due to current density (J) with electric field (E) are shown in Fig. 3(e). There is a considerable reduction in the leakage current of BFO upon Pb^{2+} doping, which may relate to the reduction in oxygen vacancies. The characteristic curves exhibit ohmic behavior at low fields and exponential behavior at moderately high fields. The maximum value of J at $E = 20$ kV cm^{-1} is 10.31, 6.27, 2.72 and 1.57 μA cm^{-2}, respectively, for BFO, BPFO5, BPFO75 and BPFO10. The nonstoichiometric and inhomogeneous structure of pure BFO can cause a high leakage current. It might be easier for the Bi atoms to evaporate from the amorphous matrix than in the nucleated grains, which fasten Bi to their crystalline sites in the structure. This could be the reason for the observed higher leakage current together with an increase of nanograin boundaries in pure and 5% Pb substituted BFO.

The local short-range magnetic ordering of BFO is G-type antiferromagnetic, that is, each Fe^{3+} spin is surrounded by six antiparallel spins on the nearest Fe neighbors. The spins are in fact not perfectly antiparallel, as there is a weak canting moment caused by the local ME coupling to the polarization. Superimposed on this canting, however, is a long-range superstructure consisting of an incommensurate spin cycloid of the antiferromagnetically ordered sublattices. Fig. 3(a–d) shows the magnetization–field (M–H) hysteresis measured at room temperature. The maximum value of magnetization, $M = 4.73$, 8.41, 2.62 and 8.99 emu g^{-1}, respectively, for BFO, BPFO5, BPFO75 and BPFO10. The variation in the magnetization values depends upon both the shape/size and antiferromagnetic interactions due to Fe^{2+}/Fe^{3+} in oxygen vacancies.[16,34] In all the cases, the magnetization is not saturated up to 5 kOe magnetic field. This behavior can be explained due to Fe–O–Fe antiferromagnetic interaction that coupled with a weak ferromagnetic component, which come from the canted Fe sublattice involving Dzyaloshinskii–Moriya (DM) interactions. Obviously, the nanostructures with increase surface-to-volume ratio have decreasing saturation magnetization. This behavior might be attributed to the spin-canting anomaly, with which fine ferromagnetic iron oxide particles are not completely saturated by large magnetic fields, or due to a spin-glass-like surface layer.[35,36] To understand the magnetic behavior in the present samples, we first noted that in BFO small amounts of Fe^{2+} ions and oxygen vacancies may exist.[7] Incidentally, BFO shows p-type conductivity, which can be understood by considering the substitution of a small amount Fe^{2+} ions in Fe^{3+} positions (acceptor doping of Fe^{3+} by Fe^{2+}). When Pb^{2+} is added to BFO, Pb^{2+} is supposed to substitute Bi^{3+} because of the closer ionic radii of Pb^{2+} and Bi^{3+}. Such acceptor doping of Bi^{3+} by Pb^{2+} is expected to reduce oxygen vacancies without the liberation of electrons.[37] Normally, the oxygen partial pressure in the ambience is sufficient to incorporate oxygen into the structure to nullify the oxygen vacancies and show p-type conductivity. The hole generated can be consumed by Fe^{2+} in the Fe^{3+} position, resulting in lower acceptor doping of Fe^{3+} by Fe^{2+} in BFO. Such superexchange interaction from Fe^{3+} to Fe^{2+} ions in oxygen vacancies can induce antiferromagnetic interactions.

Fig. 3(f) shows the variation of maximum magnetization, M, remanent magnetization, M_r and coercivity, H_c, with Pb doping. The origin of the variation of M, M_r and H_c has been further analyzed with temperature dependent zero field (ZFC) and field-cooled (FC) magnetization for Pb:BFO [Fig. 4(a–d)]. For ZFC magnetization measurements, the sample was first cooled from room temperature down to 5 K in zero field. After applying the magnetic field of 500 Oe at 5 K, the magnetization was measured during the warming cycle with the field on. For field-cooled (FC) magnetization measurements, the sample was cooled in the same field (500 Oe) down to 5 K, and the FC magnetization was measured in the warming cycle under the same field. The splitting in the ZFC and FC magnetization curves is observed in all BFO samples. This splitting of the ZFC/FC curves usually appears to be a co-existent system of the antiferromagnetic and ferromagnetic phases.[38] The magnetic order of bulk BFO at room temperature is basically G-type antiferromagnetic with a spiral spin structure.[7] However, for the BFO nanoparticles weak ferromagnetism is observed, which may arise due to the non-exact compensation of the spins with a decrease in the particle size.[39] The variations in the observed magnetic behaviors in ZFC/FC must be related to the vacancies related to the nanostructural surface. Neel proposed a model for antiferromagnetic nanoparticles based on the presence of two sublattices: one with spins up and another with spins down at the surface.[40] Any imbalance in the number of spins at the surface is the origin of a net magnetic moment in "antiferromagnetic" nanoparticles below the ordering temperature of the spins. However, with dimensions of less than 62 nm, there is a possibility of modification to the cycloidal spin structure of BFO, and that can lead to weak room temperature ferromagnetism. In the present samples, the particle size, D is observed to be above 62 nm, which results in room temperature ferromagnetism.

It is also expected that the bifurcation of ZFC/FC curves is a typical spin-glass like behavior.[41] The spin-glass state generally occurs when positions of magnetic moments or signs of neighboring coupling appear in a random manner. This combination of magnetic randomness and mixed interactions causes frustration and stochastic disorder in the corresponding energy landscape. The sharp cusp observed around 65, 20, 180 and 79 K, respectively, for BFO, BPFO5, BPFO75 and BPFO10 nanostructures in the ZFC curve is represented by the blocking temperature (T_B). The T_B here may be attributed to processes such as superparamagnetic relaxation, glass transition, T_N for antiferromagnetic to ferromagnetic transition, *etc.*[38,42] However, the ZFC curve for BPFO75 shows a decreasing trend up to 5 K after $T_B = 180$ K. This represents the reorientation of Fe^{3+} moments at peak temperature. For superparamagnetic particles at temperatures, $T < T_B$, the magnetic moment is blocked along one of the anisotropy directions and does not respond to the weak applied field, and hence, the magnetization depends on

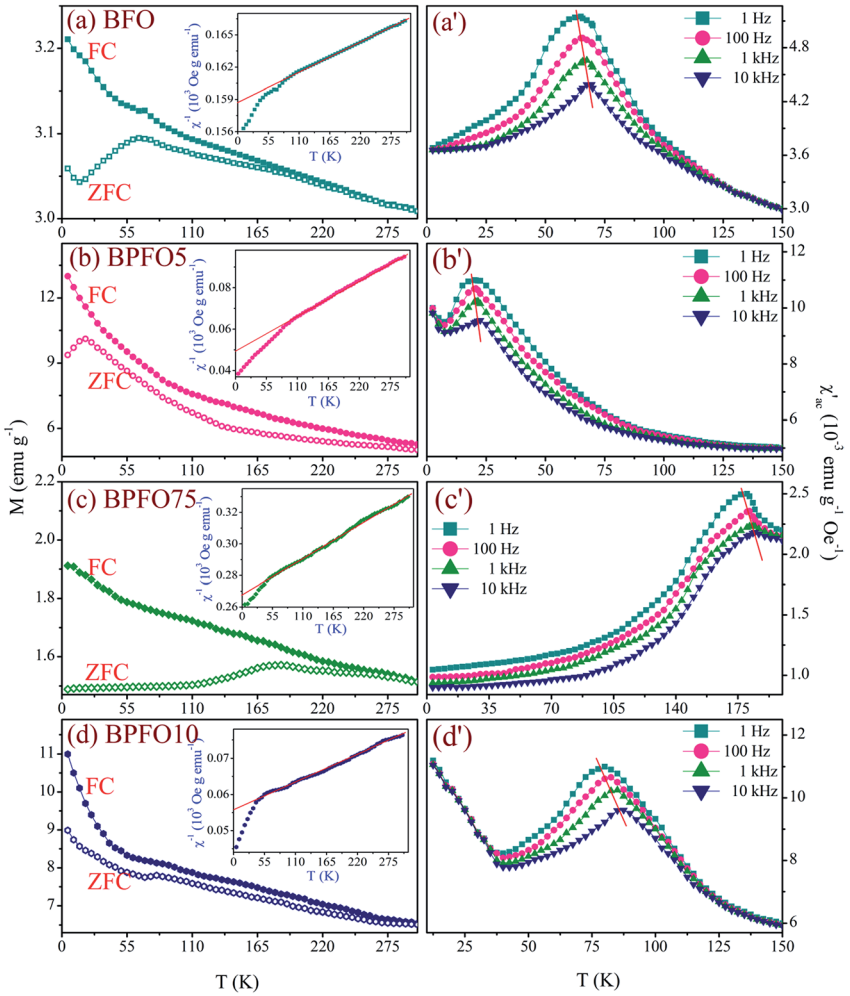

Fig. 4 (a–d) shows the magnetization, M, as a function of temperature (T) following ZFC and FC at H = 500 Oe, respectively, for Pb:BFO multiferroic systems. The respective insets of (a–d) show the $\chi^{-1}(T)$ (inversion of dc magnetic susceptibility ($\chi = M/H$) *versus* temperature) and the Curie–Weiss fittings. (a′–d′) Temperature dependent real part of the ac magnetic susceptibility (χ'_{ac}) at T = 5–200 K. The measurements were performed in an oscillating field, H_{ac} = 2.5 Oe, for frequencies 1 Hz, 100 Hz, 1 kHz and 10 kHz without any dc field bias.

magnetic history. This causes the difference in FC and ZFC magnetization. However, the superparamagnetic behavior was generally observed in small size nanoparticles.[43] This may not be the reason in the present samples because the average grain size is enhanced with Pb doping.

The enhancement in magnetization for BPFO5 and BPFO10 samples must be related to oxygen vacancies that induce Fe^{3+} to Fe^{2+} due to Pb^{2+} at the Bi^{3+} site. Coey *et al.*[44] proposed an F-center exchange mechanism model where spin-polarized electrons were trapped at oxygen vacancy sites to cause higher magnetic moments. This F-center mechanism requires clustering of the magnetic ions around vacancies. There may also be the possibility of a ferrimagnetic arrangement, in which the moments of the Fe^{2+} ions are aligned opposite to those of the Fe^{3+} ions, leading to a net magnetic moment.[45] Another possible mechanism is an increase in the canting angle of Fe ions which could be driven by the oxygen vacancies.[46]

The upward curvature observed in the FC curve in the $M(T)$ measurements [Fig. 4(a–d)] of Pb:BFO suggested a Curie–Weiss like behavior. However, the $\chi^{-1}(T)$ (inversion of susceptibility *versus* temperature) of FC curve displays [insets of Fig. 4(a–d)] a notable deviation from the Curie–Weiss law at low temperature due to the relation:

$$\chi = \frac{C}{T - \theta} \quad (1)$$

where C is the material specific Curie constant, T is the absolute temperature, and θ is the Weiss constant (in Kelvin). The Curie constants (C) have been calculated from the slope of the best fit line of the data points start below to the room temperature, and subsequently the Curie temperature, θ, is calculated. The estimated value of θ is found to be negative in all the samples which indicate the antiferromagnetic interactions.[47] Yang *et al.*[48] suggested that the negative value of θ according to eqn (1) also includes magnetic behavior such as short-range ferromagnetism, superparamagnetism or a spin-cluster character spin-disorder.

In order to understand the origin of the non-saturated magnetic hysteresis at around 5 kOe [Fig. 3], the blocking temperature observed in the ZFC [Fig. 4(a–d)] and the negative θ

values from Curie–Weiss fitting [eqn (1)], we speculated that magnetic behavior such as spin-glass may exist in Pb:BFO samples with respect to antiferromagnetic interactions. Accordingly, we measured the ac magnetic susceptibility of Pb:BFO nanostructures with frequencies 1 Hz, 100 Hz, 1 kHz 10 kHz, and the temperature dependent real (χ'_{ac}) component of ac magnetic susceptibility (χ_{ac}) is shown in Fig. 4(a′–d′). The applied oscillating field, $H_{ac} = 2.5$ Oe without any dc bias in $T =$ 5–200 K. A quite sharp cusp is observed in all the samples. The ac magnetic measurements at different frequencies reveal that the peak positions of the $\chi'_{ac}(T)$ curve shift toward higher temperature and the peak magnitudes drop down with rising frequency. Such behaviors are expected for a spin glass system; slower spin dynamics with decreasing temperature imply that spins take a longer time to relax to a relatively stable state, *i.e.*, relaxation time increases with decreasing temperature.[49] The presence of spin glass as a result of magnetic frustration can be linked to the competition between the antiferromagnetic super-exchange and the ferromagnetic double-exchange interactions.[50] An increase in dispersion in the $\chi'_{ac}(T)$ curve down to 180 K measurement in BPFO75 indicates non-interacting magnetic nanoparticles that are generally observed in an ideal superparamagnetic system.[51] Frequency dispersion in $\chi'_{ac}(T)$ around the spin glass transition has been also observed, which may occur due to clustering of glass together with the ferromagnetic and antiferromagnetic phases.[52] For the samples BPFO5 and BPFO10, $\chi'_{ac}(T)$ has frequency independent behavior at sufficiently low temperature below 20 K and starts to increase with reducing temperature. This is due to an antiferromagnetic to ferromagnetic transition. Also, the dynamic susceptibility measurements can thus be used to distinguish whether Pb:BFO is a classical spin glass or superparamagnetic by comparing the initial frequency dependence of $T_f(\omega)$ using the expression, $\Delta p = \dfrac{\Delta T_f}{T_f \Delta(\log \omega)}$.[53] The calculated peak shift (Δp) per decade of frequency shift has a value 0.014, 0.026, 0.01 and 0.019, respectively, for BFO, BPFO5, BPFO75 and BPFO10. These values of Δp are lower than those observed for the superparamagnetic system. For the non-interacting superparamagnetic material, the value of Δp is ~0.1.[54]

In order to evaluate the neutralization of oxygen vacancies and the valence stability of Fe^{2+}/Fe^{3+} in BFO with Pb doping, the oxidation states of Bi, Pb, Fe and O ions are given in Fig. 5 and 6. The investigation of the Bi 4f XPS analysis for Pb:BFO nanostructures at room temperature is given in Fig. 5(a). The doublet peak of Bi 4f that appeared at the binding energy 158.87 eV and 164.23 eV corresponding to Bi $4f_{7/2}$ and Bi $4f_{5/2}$, respectively, confirmed that the Bi ions possess a native oxidation state of +3. In addition, the calculated spin–orbit splitting energy of these doublet Bi 4f lines is around 5.36 eV, which is also consistent with the theoretical value (~5.4 eV).[55] Compared with pure BFO, the corresponding peaks in the Pb substituted BFO are shifted to the higher binding energy. This shifting in Bi 4f peak is attributed to the electronegativity of the Bi and O elements. In this case, Pb is substituted at Bi sites, whose effect can be derived from the electronegativity of the Pb ions and by evaluating the covalency/ionicity of the Bi–O and Pb–O bonds.[56] In

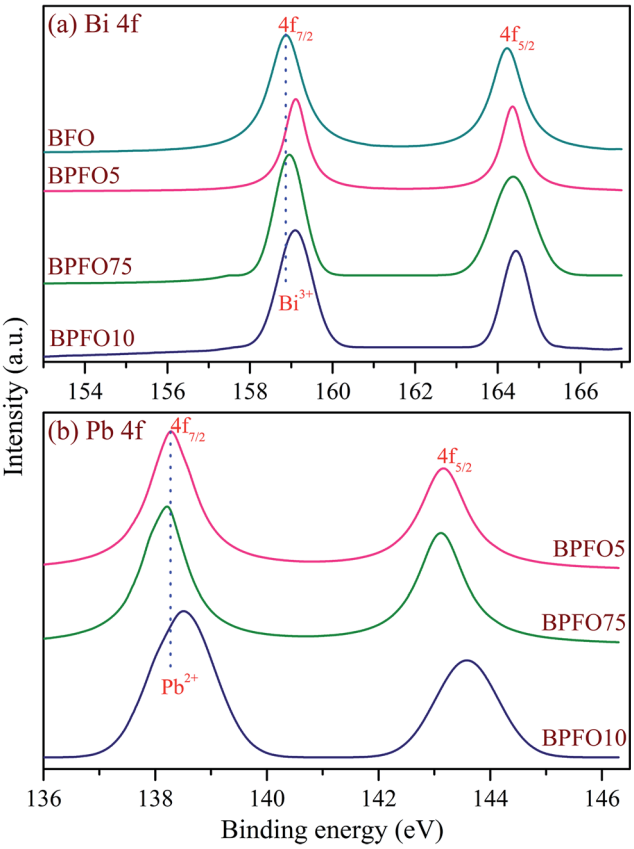

Fig. 5 XPS spectrum of (a) Bi 4f, (b) Pb 4f, measured at room temperature.

these perovskite BFO samples, Fig. 5(b) shows the Pb 4f XPS measurement that indicates that peaks for Pb $4f_{7/2}$ and $4f_{5/2}$ are found at ~138.27 and 143.15 eV, respectively. This corresponds to Pb atoms with an oxidation state of +2.[57] The shift in binding energy peaks is the successful incorporation of Pb into BFO lattice.

To evaluate the oxidation state of Fe, the XPS spectra for the Fe 2p line of Pb:BFO nanostructures is shown in Fig. 6(a–d). The XPS results showed a Fe 2p doublet consisting of a Fe $2p_{3/2}$ peak at ~710.2, 710.14, 710.07 and 710.02 eV and a Fe $2p_{1/2}$ peak at ~723.54, 723.36, 723.39 and 723.74 eV with spin–orbit splitting energy ~13.34, 13.22, 13.32 and 13.72 eV, respectively, for BFO, BPFO5, BPFO75 and BPFO10. The observed value of spin–orbit splitting energy is comparable to the theoretical ~13.6 eV.[58] It was reported[3] that Fe 2p photoelectron peaks from oxidized iron are associated with satellite (S) peaks, which are important for identifying chemical states. The Fe^{2+} and Fe^{3+} $2p_{3/2}$ peaks always show satellite peaks at 6 eV and 8 eV above the principal peaks at 709.5 eV and 711.2 eV, respectively. In Fig. 6(a–d), the satellite, S, peaks are found in the energy region 6–8 eV above the $2p_{3/2}$ principal peak. A closer examination of the Fe 2p orbital was carried out through peak fitting analysis (Gaussian fitting of Fe 2p peaks with satellites), which revealed the coexistence of Fe^{2+}/Fe^{3+} in Pb:BFO. The observed value of binding energy corresponding to Fe^{2+} and Fe^{3+} is well consistent with the reported results.[58,59] It has also been observed from Fig. 6(a–

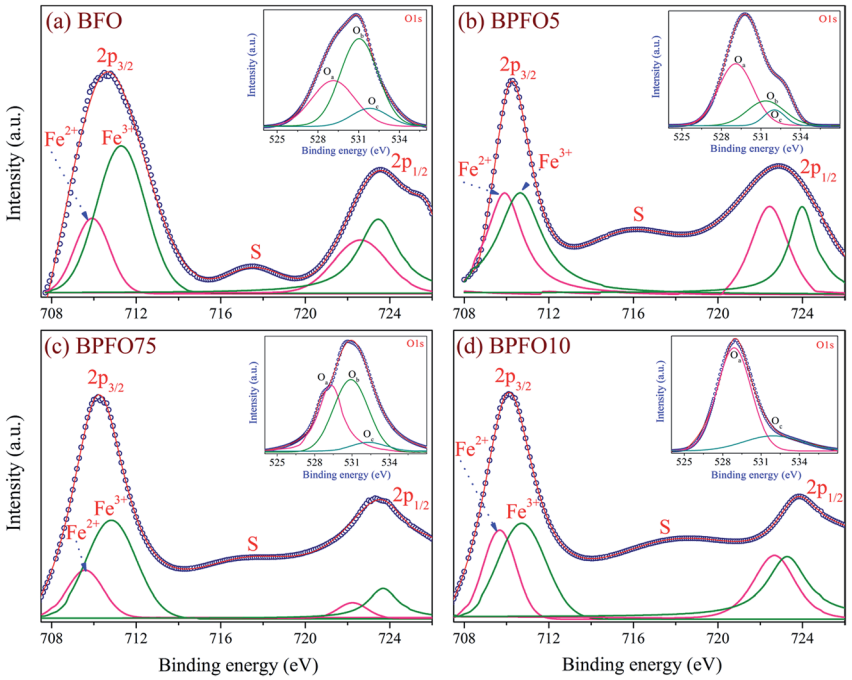

Fig. 6 (a–d) XPS spectrum at room temperature for Fe 2p [a Gaussian fitting of 2p peaks with a satellite (S) showing the splitting of Fe ions into mixed valence states +2 and +3]. Respective insets shows the Gaussian fitting for O 1s XPS spectra showing O_a, O_b and O_c peaks, respectively, related to O^{2-} ions coordinated with Pb^{2+} in BFO to induce Bi–Pb–O bonds, O^{2-} ions in the oxygen-deficient defects regions within the BFO matrix and chemisorbed oxygen on the nanostructural surface.

d) that the peak intensity and area corresponding to Fe^{3+} is higher than Fe^{2+} in both BFO and BPFO75 samples. It indicates charge fluctuation of Fe^{2+}/Fe^{3+} which might result from oxygen vacancy formation. However, the BPFO5 and BPFO10 samples have equally formed $Fe^{2+/}Fe^{3+}$ peaks. It is well known that the increase in the macroscopic magnetization of BFO based materials may attributed to the existence of Fe^{2+} ions.[60] The concentration of Fe^{2+} ions in BPFO5 and BPFO10 is higher and shown comparatively higher magnetization [Fig. 3].

The insets of Fig. 6(a–d) show the O 1s spectra for Pb:BFO nanostructures at room temperature. The O 1s spectra of pure BFO is found to be asymmetric, which indicates imbalances occur in its stoichiometric ratio to change the oxidation state. This eventually induces defects in the BFO and they are often found to be oxygen vacancies.[61] Accordingly, the Gaussian fitted oxygen spectra, as shown in the respective inset of Fig. 6(a–d), reveal the peaks. The peak located on the low binding energy side (O_a) is attributed to O^{2-} ions on the perovskite BFO phase.[62] The O_b can be attributed to oxygen vacancy/defect formation. The O_c peak is usually attributed to chemisorbed oxygen on the surface of the nanostructures. For pure BFO, the value of O_a is ~528.91 eV, O_b ~ 531.18 eV and O_c ~ 531.97 eV. It has been observed that the peak area of oxygen vacancies related to O_b is reduced with Pb doping and diminished at higher Pb concentrations (BPFO10). Consequently, O_a is enhanced with Pb doping. This means that the dopant ions could neutralize the oxygen vacancies as well convert them into Fe^{2+}/Fe^{3+} valences equally in the BFO lattice.

Fig. 7(a–d) shows the magnetic field affected dielectric behavior of Pb:BFO nanostructures measured at room temperature. It shows frequency dependent relative permittivity (ε_r) of Pb:BFO in the frequency region 20 Hz to 10 MHz under the influence of a direct magnetic field (H = 0, 1 kOe). In Fig. 7(a–d), all Pb:BFO nanostructures show variation in the dielectric constant and tan δ (respective insets) at the low frequency region. The dielectric constant with a large value at low frequencies decreases with increasing frequency and is nearly constant at high frequencies. This phenomenon can be attributed to the Maxwell–Wagner-type contribution to the dielectric constant. This phenomenon is related to the space charge relaxation at the interface. The space charges are suggested to originate from oxygen vacancies and Bi vacancies, *etc.*[63] At low frequencies, the space charges can follow the applied electric field and contribute to the dielectric constant, while at high frequencies, they do not have time to build up and undergo relaxation. Jaiswal *et al.*[64] suggested the low frequency dispersion in ε and tan δ was due to the presence of polarization factors such as interfacial, dipolar, ionic, atomic, and electronic effects which become significant at low frequencies. Without applying a field H, the value of ε at 1 MHz is 5.1, 1.8, 10.6 and 12, respectively, for BFO, BPFO5, BPFO75 and BPFO10 nanostructures. The value of ε at 1 kHz is also given (Table 2).

The improvement of the dielectric constant with the substitution of Pb^{2+} for Bi^{3+} provides a larger vibration space to a larger dipole moment.[65] Besides the oxygen vacancies that are compensated due to formation of Fe^{2+}/Fe^{3+} valence states have minor effect on dielectric behavior. The shape/size of BFO grains are also influenced the dielectric properties [Fig. 7(a–d)]. An increase in grain/crystallite size will lead to a decrease in the internal stresses, resulting in an increased dielectric constant.[66]

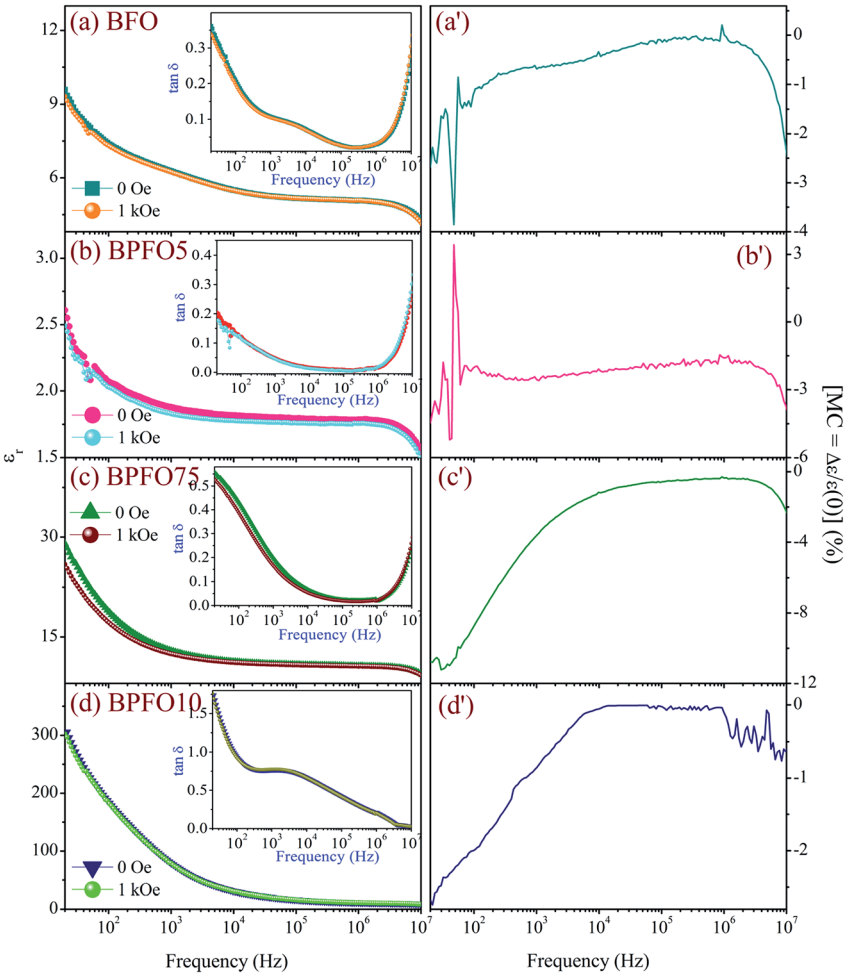

Fig. 7 (a–d) Frequency dependent relative permittivity (ε_r) (respective insets are loss (tan δ)) at magnetic field $H = 0$, 1 kOe measured at room temperature for Pb:BFO multiferroics. (a′–d′) Calculation for magnetocapacitance [MC = change in dielectric constant (ε), $[\varepsilon(H) - \varepsilon(0) = \Delta\varepsilon]/\varepsilon(0)$, where $\varepsilon(H)$ and $\varepsilon(0)$ denotes the dielectric constants at an applied dc bias magnetic field H and zero field].

In addition, grain boundaries pinning the domain wall motion can influence the dielectric response and further affect the dielectric constant.[67] Also, it is clearly understood that the capacitance varies with applying magnetic field. This variation of capacitance with increase in magnetic field indicates a positive/negative magneto-dielectric/capacitance, MD/MC effect. The appearance of any polarity, negative or positive sign of the MD effect is determined by the product of the spin pair correlation of neighboring spins and the coupling constant.[68]

In order to understand the mechanism of ME coupling between electric and magnetic order in Pb:BFO samples, we have measured capacitance at $H = 0$, 1 kOe as a function of frequency (MD/MC), shown in Fig. 7(a′–d′). The ME coupling in multiferroics can be confirmed by (i) a change or an anomaly in the temperature dependence dielectric constant, ε, across a magnetic transition (T_N) and/or (ii) a change in ε as well induced voltage by the application of magnetic fields.[69] To establish the second criterion, the frequency-dependent capacitance at magnetic field $H = 0$, 1 kOe has been checked at room temperature. The significant and systematic variation of capacitance with increase in the applied static magnetic field throughout the frequency range of investigation implies the existence of strong ME coupling. The decrease in capacitance with increase in magnetic field indicates a negative magneto-capacitance, MC, effect. This effect is achieved through a combination of magnetoresistance and the Maxwell–Wagner effect.[70] This MC contributes the magnetostrictive effect which might induce a change in size of the magnetic nanoparticles under an applied magnetic field. It would lead to local stresses (or strains) and a consequent change in polarization of the ferroelectric phase due to the piezoelectric effect. It is observed that MC changes dramatically as the frequency increases, which indicates charge relaxation in a magnetic field as well as the dependence of spin relaxation upon the magnetic field.[71] Any changes in resistance of either the grain or grain boundary phase induce polarization, and the MC effect might arising from the spin polarized tunneling across grain boundaries. The antiferromagnetic to ferromagnetic transition (depending on the magnetic state suggested by Imamura *et al.*[72]) in Fig. 4 is also responsible for a negative MC effect. The values of MC $\{[\varepsilon(H) - \varepsilon(0) = \Delta\varepsilon]/\varepsilon(0)\}$ at a frequency of 1 MHz is 0.61, 1.59,

0.36 and 0.11%, respectively, calculated for BFO, BPFO5, BPFO75 and BPFO10.

Fig. 8 shows the temperature dependent relative permittivity (ε_r) for Pb:BFO nanostructures. It clearly demonstrates that the dielectric permittivity increases with increase in temperature. It has been observed that ε_r increases gradually with increase in temperature to its maximum value (ε_{max}) and then decreases slightly. Furthermore, the value of ε_r starts to increase with temperature because the T_c for pure BFO is 1103 K. This change in ε_r at 600–650 K for all Pb:BFO samples occurs in the range of the occurrence of T_N. For pure BFO, the value of T_N is 643 K. The value of the ferroelectric phase transition temperature (T_{FE}) is 644, 631, 649 and 629 K, respectively, for BFO, BPFO5, BPFO75 and BPFO10. This observation is an anomaly in the phase transition; T_{FE} around T_N confirms the ME coupling, which is of intrinsic multiferroic origin, must be correlated with inverse DM-type interactions. It occurs in complex magnetic structures such as noncollinear canted antiferromagnets, where the canted spin polarizes the off-center orbital through electron–lattice interaction. This anomaly could be due to ME coupling and can be explained in the framework of the Landau–Devonshire theory of phase transition in magneto-electrically ordered systems.[73]

Moreover, a step-like increase in ε_r at moderate temperatures (around 600–650 K), whose height decreases and position shifts to high temperatures with frequency (except for pure BFO) is observed. The variation in phase transition temperature with frequency for Pb:BFO nanostructures is given in Fig. 8(a–d), respectively. The emergence of the relaxor behavior in this study may explained by the increased cation disorder in the B-site and Bi-site substituted by Pb^{2+}. Due to the size and charge difference, the substitutions disrupt the long-range dipolar interaction and form the local distortion of the polar region.[74] These isolated clusters of polar nano regions (PNRs), which result from the inhomogeneous composition and charge difference, are weak couplings between neighboring clusters.[75] The interaction among the PNRs leads to a high random field and affects the relaxor behavior. It is generally accepted that PNRs play a crucial role in relaxor behavior.

4. Conclusion

We have synthesized multiferroic $Bi_{1-x}Pb_xFeO_3$ nanostructures by chemical combustion and annealing at 500 °C/5 h. The XRD pattern results in a crystalline rhombohedral BFO structure which is also induced to the tetragonal phase with Pb doping. The Pb dopant ions in BFO cause lattice distortion and expansion in the unit cell to induce lattice strain. The FESEM images show BFO nanoparticles ($D = 75 \pm 2$ nm), BPFO5 cubic shaped nanoparticles ($D = 400 \pm 15$ nm), and high-Pb-doped nanorods ($D = 102 \pm 5$ nm and 125 ± 4 nm, and length, $L = 510 \pm 15$ nm and 900 ± 20 nm, respectively, for BPFO75 and BPFO10). The lattice strain due to distortion and expansion and nanostructural shape/size in Pb:BFO could result in ferroelectric polarization, $P_s = 0.75$, 1.76, 3.55 and 6.73 μC cm^{-2}, respectively, for BFO, BPFO5, BPFO75 and BPFO10. The valence in conversion of Fe^{3+} to Fe^{2+} due to oxygen vacancies results in enhancement of antiferromagnetic–ferromagnetic interactions in Pb:BFO. At room temperature, the maximum values of magnetization are 4.73, 8.41, 2.62 and 8.99 emu g^{-1}, respectively, for BFO, BPFO5, BPFO75 and BPFO10. The present BFO nanostructures have magnetic spins that are contributed by

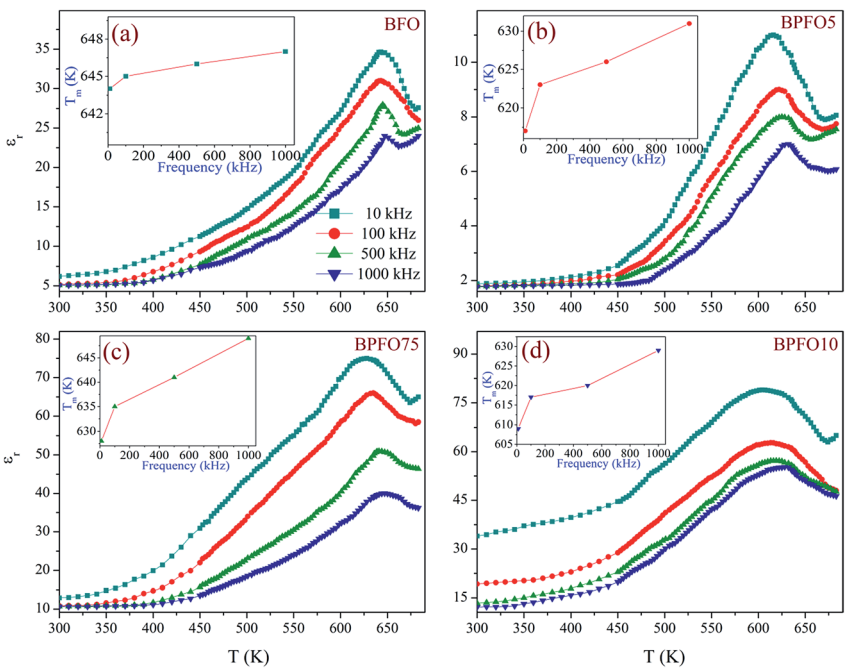

Fig. 8 Temperature dependent relative permittivity (ε_r) of the Pb:BFO multiferroics to indicate a ferroelectric phase transition near the antiferromagnetic T_N of the host material BFO. Insets (a–d) show variation of phase transition temperature with frequency, respectively.

antiferromagnetism, spin glasses and superparamagnetic interactions that were studied by ZFC/FC measurements, Curie–Weiss fitting (extract negative θ value) and ac magnetic susceptibility, $\chi'_{ac}(T)$. XPS analysis shows oxidation states of Bi (+3), Pb (+2), Fe (+2/+3) and oxygen vacancies that are reduced with doping of Pb. The dielectric measurement with applied magnetic field $H = 0$, 1 kOe induces strong ME coupling as revealed by MC study. The dielectric anomaly due to the ferroelectric phase transition near T_N could further confirm the ME coupling effect. Overall, the ME, ferroelectric and ferromagnetic behaviors in the Pb substituted BFO multiferroic samples are highly influenced by oxygen vacancy defects.

Acknowledgements

This work was financially supported by the SERB Department of Science and Technology, Government of India under the Fast Track Scheme for Young Scientists (SB/FTP/PS-180/2013). The author Kuldeep Chand Verma is also grateful to the Chairperson, Department of Physics, Panjab University, Chandigarh, for providing constant encouragement, motivation, and support to carry out this study.

References

1 T. Kimura, T. Goto, H. Shintani, K. Ishizaka, T. Arima and Y. Tokura, *Nature*, 2003, **426**, 55.
2 H. W. Chang, F. T. Yuan, K. T. Tu, Y. C. Lo, S. Y. Tu, C. R. Wang, A. B. Yang, C. S. Tu, S. U. Jen and W. C. Chang, *J. Appl. Phys.*, 2015, **117**, 17C734.
3 K. C. Verma, S. K. Tripathi and R. K. Kotnala, *RSC Adv.*, 2014, **4**, 60234.
4 B. Cui, C. Song, H. Mao, H. Wu, F. Li, J. Peng, G. Wang, F. Zeng and F. Pan, *Adv. Mater.*, 2015, **27**, 6651.
5 J. S. Hwang, J. Y. Cho, S. Y. Park, Y. J. Yoo, P. S. Yoo, B. W. Lee and Y. P. Lee, *Appl. Phys. Lett.*, 2015, **106**, 062902.
6 F. Yan, G. Xing, R. Wang and L. Li, *Sci. Rep.*, 2015, **5**, 9128.
7 D. P. Dutta, O. D. Jayakumar, A. K. Tyagi, K. G. Girija, C. G. S. Pillai and G. Sharma, *Nanoscale*, 2010, **2**, 1149.
8 K. Kalantari, I. Sterianou, S. Karimi, M. C. Ferrarelli, S. Miao, D. C. Sinclair and I. M. Reaney, *Adv. Funct. Mater.*, 2011, **21**, 3737.
9 C. M. Raghavan, J. W. Kim and S. S. Kim, *J. Am. Ceram. Soc.*, 2014, **97**, 235.
10 X. Qi, J. Dho, R. Tomov, M. G. Blamire and J. L. MacManus-Driscoll, *Appl. Phys. Lett.*, 2005, **86**, 062903.
11 V. V. Lazenka, A. F. Ravinski, I. I. Mokoed, J. Vanacken, G. Zhang and V. V. Moshchalkov, *J. Appl. Phys.*, 2012, **111**, 123916.
12 Q. Jiang, H. Ning, Q. Zhang, M. Cain, M. J. Reece and H. Yan, *J. Mater. Chem.*, 2013, **1**, 5628.
13 J. Rout and R. N. P. Choudhary, *Phys. Lett. A*, 2016, **380**, 288.
14 J. Wei, R. Haumont, R. Jarrier, P. Berhtet and B. Dkhil, *Appl. Phys. Lett.*, 2010, **96**, 102509.
15 J. K. Kim, S. S. Kim, E. J. Choi, W. J. Kim, A. S. Bhalla and T. K. Song, *J. Korean Phys. Soc.*, 2006, **49**, 566.
16 K. C. Verma and R. K. Kotnala, *Mater. Chem. Phys.*, 2016, **174**, 120.
17 A. R. Makhdoom, M. J. Akhtar, M. A. Rafiq, M. Siddique, M. Iqbal and M. M. Hasan, *AIP Adv.*, 2014, **4**, 037113.
18 P. Nayek and G. Li, *Sci. Rep.*, 2015, **5**, 10845.
19 K. C. Verma and R. K. Kotnala, *J. Am. Ceram. Soc.*, 2016, **99**(5), 1601.
20 L. Ju, T. Sabergharesou, K. G. Stamplecoskie, M. Hegde, T. Wang, N. A. Combe, H. Wu and P. V. Radovanovic, *J. Am. Chem. Soc.*, 2012, **134**, 1136.
21 D. H. Wang, W. C. Goh, M. Ning and C. K. Ong, *Appl. Phys. Lett.*, 2006, **88**, 212907.
22 T. P. Comyn, T. Stevenson, M. Al-Jawad, S. L. Turner, R. I. Smith, W. G. Marshall, A. J. Bell and R. Cywinski, *Appl. Phys. Lett.*, 2008, **93**, 23.
23 K. C. Verma and R. K. Kotnala, *Mater. Res. Express*, 2016, **3**(5), 055006.
24 J. Iqbal, T. Jan, Y. Ronghai, S. H. Naqvi and I. Ahmad, *Nano-Micro Lett.*, 2014, **6**(3), 242.
25 G. Cao and W. Ying, *Nanostructures and Nanomaterials: Synthesis, Properties, and Applications*, World Scientific, Singapore, 2nd edn, 2004, vol. 2.
26 R. E. Cohen, *Nature*, 1992, **358**, 136.
27 N. A. Hill, *J. Phys. Chem. B*, 2000, **104**, 6694.
28 H. Zhao, J. Wang, L. Zhang, Y. Rong, J. Chen, K. Ibrahim and X. Xing, *Dalton Trans.*, 2013, **42**, 10358.
29 C. X. Li, B. Yang, S. T. Zhang, D. Q. Liu, R. Zhang, Y. Sun and W. W. Cao, *J. Alloys Compd.*, 2014, **590**, 346.
30 E. A. Eliseev, A. N. Morozovska, M. D. Glinchuk and R. Blinc, *Phys. Rev. B: Condens. Matter Mater. Phys.*, 2009, **79**, 165433.
31 Z. Wu and R. E. Cohen, *Phys. Rev. Lett.*, 2005, **95**, 037601.
32 B. Sun, P. Han, W. Zhao, Y. Liu and P. Chen, *J. Phys. Chem. C*, 2014, **118**, 18814.
33 D. Li, W. Zheng, D. Zheng, J. Gong, L. Wang, C. Jin, P. Li and H. Bai, *ACS Appl. Mater. Interfaces*, 2016, **8**, 3977.
34 D. P. Dutta, B. P. Mandal, M. D. Mukadam, S. M. Yusuf and A. K. Tyagi, *Dalton Trans.*, 2014, **43**, 7838.
35 A. Hajalilou, M. Hashim, R. Ebrahimi, H. M. Kamari and N. Sarami, *Ceram. Int.*, 2014, **40**, 5881.
36 R. H. Kodima, A. E. Berkowitz, J. E. J. McNiff and S. Foner, *Phys. Rev. Lett.*, 1996, **77**, 394.
37 R. Mazumder and A. Sen, *J. Alloys Compd.*, 2009, **475**, 577.
38 K. C. Verma and R. K. Kotnala, *Phys. Chem. Chem. Phys.*, 2016, **18**, 5647.
39 J. C. Denardin, A. L. Brandl, M. Knobel, P. Panissod, A. B. Pakhomov, H. Liu and X. X. Zhang, *Phys. Rev. B: Condens. Matter*, 2002, **65**, 064422.
40 L. Neel, in *Low Temperature Physics*, ed. C. Dewitt, B. Dreyfus and P. D. de Gennes, Gordon and Beach, New York, 1962, p. 413.
41 C. J. Cheng, C. Lu, Z. Chen, L. You, L. Chen, J. Wang and T. Wu, *Appl. Phys. Lett.*, 2011, **98**, 242502.
42 G. Catalan and J. F. Scott, *Adv. Mater.*, 2009, **21**, 2463.
43 K. L. Da Silva, D. Menzel, A. Feldhoff, C. Kubel, M. Bruns, A. Paesano Jr, A. Duvel, M. Wilkening, M. Ghafari, H. Hahn, F. J. Litterst, P. Heitjans, K. D. Becker and V. Sepelak, *J. Phys. Chem. C*, 2011, **115**, 7209.

44 J. M. D. Coey, A. P. Douvalis, C. B. Fitzgerald and M. Venkatesan, *Appl. Phys. Lett.*, 2004, **84**, 1332.
45 J. Wang, A. Scholl, H. Zheng, S. B. Ogale, D. Viehland, D. G. Schlom, N. A. Spaldin, K. M. Rabe, M. Wuttig, L. Mohaddes, J. Neaton, U. Waghmare, T. Zhao and R. Ramesh, *Science*, 2005, **307**, 1203b.
46 G. Chen, C. Song, C. Chen, S. Gao, F. Zeng and F. Pan, *Adv. Mater.*, 2012, **24**, 3515.
47 S. Basu, D. Y. Inamdar, S. Mahamuni, A. Chakrabarti, C. Kamal, G. R. Kumar, S. N. Jha and D. Bhattacharyya, *J. Phys. Chem. C*, 2014, **118**, 9154.
48 C. Y. Yang, Y. H. Lu, W. H. Lin, M. H. Lee, Y. J. Hsu and Y. C. Tseng, *J. Phys. D: Appl. Phys.*, 2014, **47**, 345003.
49 J. Xing, Z. Zhang, Z. Zheng, Z. Wang, W. Huang and G. Liu, *J. Appl. Phys.*, 2013, **113**, 233912.
50 B. Cui, C. Song, G. Y. Wang, H. J. Mao, F. Zeng and F. Pan, *Sci. Rep.*, 2013, **3**, 2542.
51 S. Lin, D. F. Shao, J. C. Lin, L. Zu, X. C. Kan, B. S. Wang, Y. N. Huang, W. H. Song, W. J. Lu, P. Tong and Y. P. Sun, *J. Mater. Chem. C*, 2015, **3**, 5683.
52 S. S. Rathore and S. Vitta, *Sci. Rep.*, 2015, **5**, 9751.
53 S. Mukherjee, A. Garg and R. Gupta, *Appl. Phys. Lett.*, 2012, **100**, 112904.
54 L. Ma, W. H. Wang, J. B. Lu, J. Q. Li, C. M. Zhen, D. L. Hou and G. H. Wu, *Appl. Phys. Lett.*, 2011, **99**, 182507.
55 S. Bharathkumar, M. Sakar and S. Balakumar, *Phys. Chem. Chem. Phys.*, 2015, **17**, 17745.
56 A. Tamilselvan, S. Balakumar, M. Sakar, C. Nayek, P. Murugavel and K. S. Kumar, *Dalton Trans.*, 2014, **43**, 5731.
57 T. W. Ng, C. Y. Chan, M. F. Lo, Z. Q. Guan and C. S. Lee, *J. Mater. Chem. A*, 2015, **3**, 9081.
58 F. Moulder, W. F. Stickle, P. E. Sobol and K. D. Bomben, *Handbook of X-Ray Photoelectron Spectroscopy*, Perkin-Elmer, Minnesota, 1992.
59 B. A. Kobe, A. P. Grosvenor, M. C. Biesinger and N. S. McIntyre, *Surf. Interface Anal.*, 2004, **36**, 1564.
60 Z. Hu, M. Li, B. Yu, L. Pei, J. Liu, J. Wang and X. Zhao, *J. Phys. D: Appl. Phys.*, 2009, **42**, 185010.
61 A. Lahmar, K. Zhao, S. Habouti, M. Dietze, C. H. Solterbeck and M. E. Souni, *Solid State Ionics*, 2011, **202**, 1.
62 R. Das, T. Sarkar and K. Mandal, *J. Phys. D: Appl. Phys.*, 2012, **45**, 455002.
63 Y. F. Cui, Y. G. Zhao, L. B. Luo, J. J. Yang, H. Chang, M. H. Zhu, D. Xie and T. L. Ren, *Appl. Phys. Lett.*, 2010, **97**, 222904.
64 A. Jaiswal, R. Das, T. Maity, K. Vivekanand, S. Adyanthaya and P. Poddar, *J. Phys. Chem. C*, 2010, **114**, 12432.
65 W. Sun, J. F. Li, Q. Yu and L. Q. Cheng, *J. Mater. Chem. C*, 2015, **3**, 2115.
66 J. Perez de la Cruz, E. Joanni, P. M. Vilarinho and A. L. Kholkin, *J. Appl. Phys.*, 2010, **108**, 114106.
67 F. Xu, S. T. McKinstry, W. Ren, B. M. Xu, Z. L. Xie and K. J. Hemker, *J. Appl. Phys.*, 2001, **89**, 1336.
68 D. K. Pradhan, V. S. Puli, S. Kumari, S. Sahoo, P. T. Das, K. Pradhan, D. K. Pradhan, J. F. Scott and R. S. Katiyar, *J. Phys. Chem. C*, 2016, **120**, 1936.
69 R. Schmidt, J. Ventura, E. Langenberg, N. M. Nemes, C. Munuera, M. Varela, M. Hernandez, C. Leon and J. Santamaria, *Phys. Rev. B: Condens. Matter Mater. Phys.*, 2012, **86**, 035113.
70 T. Goto, T. Kimura, G. A. Lawes, P. Ramirez and Y. Tokura, *Phys. Rev. Lett.*, 2004, **92**, 257201.
71 Y. Chen, X. Y. Zhang, C. Vittoria and V. G. Harris, *Appl. Phys. Lett.*, 2009, **94**, 102906.
72 N. Imamura, M. Karppinen, T. Motohashi, D. Fu, M. Itoh and H. Yamauchi, *J. Am. Chem. Soc.*, 2008, **130**, 14948.
73 K. C. Verma and R. K. Kotnala, *Solid State Commun.*, 2011, **151**, 920.
74 S. N. Tripathy, K. K. Mishra, S. Sen, B. G. Mishra, D. K. Pradhan, R. Palai and D. K. Pradhan, *J. Appl. Phys.*, 2013, **114**, 144104.
75 X. Huang, H. Hao, S. Zhang, H. Liu, W. Zhang, Q. Xu and M. Cao, *J. Am. Ceram. Soc.*, 2014, **97**, 1797.

